Correlating hydration free energy and specific adsorption of alkali metal cations during CO_2 electroreduction on Au

Vincent J. Ovalle[1], Yu-Shen Hsu[1], Naveen Agrawal[2], Michael J. Janik[2*] and Matthias M. Waegele[1*]

[1*]Department of Chemistry, Merkert Chemistry Center, Boston College, Chestnut Hill, 02467, Massachusetts, United States.
[2*]Department of Chemical Engineering, The Pennsylvania State University, University Park, 16802, Pennsylvania, United States.

*Corresponding author(s). E-mail(s): mjj13@psu.edu; waegele@bc.edu;

Abstract

Specifically adsorbed alkali metal cations on metal electrodes have been hypothesized to influence the reduction of CO_2. However, experimental detection of these cations during CO_2 reduction has remained elusive. Herein, employing the asymmetric CH_3 deformation band of tetramethylammonium ($methyl_4N^+$) as a vibrational probe of the aqueous electrolyte/polycrystalline Au interface, we monitored the displacement of specifically adsorbed $methyl_4N^+$ by alkali metal cations. We found that the coverage of specifically adsorbed alkali metal cations during CO_2-to-CO reduction follows the order $Li^+ < Na^+ < K^+ < Cs^+$, for the same bulk concentration. The alkali metal cations' experimentally observed surface coverages correlate with their free energies of hydration. Further, the rate of CO_2-to-CO conversion increases with the coverage of specifically adsorbed alkali metal cations. Our observations suggest that the degree to which alkali metal cations undergo partial dehydration at the electrode/electrolyte interface plays a key role in their ability to promote CO_2-to-CO reduction.

1 Introduction

The structure of the electrode-electrolyte interface, or electrochemical double layer (EDL), is of great fundamental and practical interest. [1–4] According to classic theories, which are based on continuum electrostatics, the distribution of ions in the EDL is determined by electrostatic interactions between the surface charge on the electrode and ions in the electrolyte. [5] Analysis of the EDL with modern experimental and computational techniques has demonstrated the limits of the continuum electrostatics description and has revealed that the distribution of ions in the EDL arises from a complex interplay between various competing intermolecular and interfacial forces that depend on the physical and chemical properties of solvent, ions, and electrode. [1–4, 6–12] Although significant progress has been made in understanding the structure of the EDL in model systems, the distribution of ions in the EDL under catalytically relevant conditions remains poorly understood. Because the catalytic activity of the interface is influenced by ions in its immediate vicinity, there exists a strong need for experiments that probe the distribution of ions in the EDL under reaction conditions. In this context, the role of cations in the EDL is of particular interest.

For almost a century, it has been known that cations of the supporting electrolyte can alter the rates and product selectivity of electrocatalytic reactions. [4, 13–15] Such cation effects provide an opportunity for tailoring electrolyte/electrode interfaces that can selectively and efficiently catalyze challenging reactions, such as CO_2 reduction, [16, 17] nitrogen and nitrate reduction, [18, 19] or water oxidation. [20, 21] For example, during the reduction of CO_2 on Cu(100) electrodes at a potential of -1.1 V versus the reversible hydrogen electrode (RHE), the rate of ethylene evolution was found to increase by a factor of $\sim$3.75 upon switching from 0.1 M $LiHCO_3$ to 0.1 M $CsHCO_3$ electrolyte. [22] For water oxidation on RuO_2(110), the activation barrier of the reaction at an overpotential of 0.32 V was found to drop from 0.53 eV in 0.1 M LiOH to 0.42 eV in 0.1 M KOH. [23] The mechanisms by which cations modulate the free energy landscapes of electrocatalytic reactions are still under debate. [4] Proposed mechanisms include site-blocking, [24–26] chemical and/or electrostatic interactions with adsorbates, [27–35] modulation of the interfacial pH, [36–38] and changes in water structure. [39, 40] Typically, multiple mechanisms are expected to be simultaneously operational under a given set of conditions. [41–43] By their nature, these mechanisms are intimately tied to the distribution of cations in the EDL. Of particular interest is the question if specifically adsorbed alkali metal cations, that is, partially dehydrated cations in direct contact with the electrode surface, exist under catalytically relevant conditions. If present, specifically adsorbed cations are expected to have a significant impact on electrocatalytic processes such as CO_2 reduction because they could chemically or electrostatically interact with surface-adsorbed reaction intermediates. [28] The presence of specifically adsorbed alkali metal cations at electrode potentials relevant for CO_2 reduction

has been predicted by DFT calculations, [28, 44] but has not been experimentally confirmed to date. Similarly, specifically adsorbed cations on Pt electrodes have been theorized to affect hydrogen oxidation/evolution. [30, 44–46] A key challenge in this regard it the dearth of techniques capable of probing the distribution of alkali metal cations in the EDL under catalytic conditions.

Low energy electron diffraction and Auger spectroscopy have provided surface coverages and structures of adlattices of alkali and alkaline earth metal cations on single crystal electrodes. [47, 48] However, these techniques require removal of the electrode from the electrolyte prior to surface characterization. In these pioneering studies, it was assumed that the EDL is preserved upon transfer from the liquid electrolyte to the ultra-high vacuum environment. More recently, surface x-ray diffraction studies have provided detailed structural information about alkali metal cations at electrodes immersed in aqueous electrolytes. [49–52] However, application of these techniques to catalytically relevant potential regimes remains to be demonstrated. Vibrational Stark spectroscopy can measure the electrolyte-dependent interfacial electric field, [29, 39, 41, 42, 53–55] but cannot directly probe specifically adsorbed alkali metal cations.

Herein, we provide experimental evidence of specifically adsorbed alkali metal cations on polycrystalline Au electrodes under CO_2-to-CO conversion. Using surface-enhanced infrared absorption spectroscopy (SEIRAS) on polycrystalline Au electrodes, we established tetramethylammonium ($methyl_4N^+$) as a vibrational probe of the relative surface coverage of specifically adsorbed alkali metal cations. By monitoring the asymmetric CH_3 deformation mode of $methyl_4N^+$, we discovered two distinct sub-populations of this cation, hydrated $methyl_4N^+$ and specifically adsorbed $methyl_4N^+$ ($methyl_4N_{ads}$). With SEIRAS, we observed that alkali metal cations displace $methyl_4N_{ads}$ from the electrode, thereby rendering the asymmetric CH_3 deformation band of $methyl_4N_{ads}$ an experimental probe of the relative coverage of specifically adsorbed alkali metal cations on the electrode. For the same bulk concentration of alkali metal cations, we determined that the coverages of specifically adsorbed cations increase in the order $Li^+ < Na^+ < K^+ < Cs^+$. The spectroscopically determined relative surface coverages correlate with the alkali metal cations' free energies of hydration. That is, the less tightly bound the hydration shell of an alkali metal cation is, the higher its surface coverage. Further, we determined that the rate of CO_2-to-CO conversion monotonically increases with the coverage of specifically adsorbed alkali metal cations. This observation indicates that partial dehydration of alkali metal cations is a critical factor in their ability to promote the CO_2 reduction reaction.

2 Results

Dependence of line shape of CH_3 deformation band on EDL. To investigate the potential-dependent behavior of $methyl_4N^+$ at the polycrystalline Au/electrolyte interface, we probed the asymmetric CH_3 deformation

mode (ν_{as}) [56] of this cation with SEIRAS in the attenuated total reflectance (ATR) configuration. Figure 1 shows representative spectra collected during the cathodic forward scans of cyclic voltammograms of Au electrodes in CO_2-saturated electrolytes containing 100 mM $methyl_4N^+$, 90 mM $methyl_4N^+$ and 10 mM K^+, and 50 mM $methyl_4N^+$ and 50 mM K^+ and bicarbonate as the common counterion. The nominal turning potentials were +0.2 and −1.1 V and the scan rate was 2 mV s^{-1}. Unless otherwise indicated, all potentials in this article are referenced against RHE. The corresponding electrochemical current densities and reverse scans are provided in Supplementary Figure 1. The spectra are difference spectra. That is, they report changes of the interface with respect to a reference state. The reference state is the state of the interface at the reference potential of +0.2 V. The change in optical density (OD) was calculated according to $\Delta\text{mOD} = -10^3 \log_{10} \frac{S}{R}$, where S and R refer to the single-beam spectra at the sample and reference potentials, respectively. Further experimental details are provided in the Methods section.

The lineshape of ν_{as} of $methyl_4N^+$ exhibits a remarkable dependence on electrolyte composition; when $methyl_4N^+$ is the only cation in the electrolyte, a prominent positive-going band at ∼1490 cm^{-1} appears with decreasing potential (Figure 1A). By contrast, in the presence of 10 mM K^+, a biphasic feature with a positive-going band at ∼1490 cm^{-1} and a negative-going band at ∼1482 cm^{-1} develops (Figure 1B). In the presence of 50 mM K^+, only the negative-going band at ∼1482 cm^{-1} is evident (Figure 1C). The development of the spectral features is highly reversible, as evidenced by the disappearance of the peaks during the reverse scans of the cyclic voltammograms with no appreciable hysteresis (Supplementary Figure 1). The reproducibility of the results is demonstrated by the independent, duplicate experiment in Supplementary Figure 2.

The two bands suggest the presence of two spectroscopically distinguishable populations of $methyl_4N^+$ at the Au/electrolyte interface. To gain insights into these distinct populations, we plotted the spectra at −0.8 V in the different electrolytes from Figure 1 in Figure 2 for direct comparison. Comparison of the SEIRAS spectra with ν_{as} of $methyl_4N^+$ in bulk solution (green dashed spectrum in Figure 2) shows that the positive-going band at ∼1490 cm^{-1} is attributable to the accumulation of hydrated $methyl_4N^+$ in the EDL with decreasing electrode potential. This assignment is further supported by the observation that the band's amplitude increases with increasing concentration of $methyl_4N^+$ and decreasing concentration of K^+ (Figure 2).

We now turn to the band at ∼1482 cm^{-1}, which characterizes a distinct $methyl_4N^+$ population at the interface. As detailed below, our experimental evidence suggests that this band arises from the displacement of specifically adsorbed $methyl_4N^+$ by K^+ with decreasing potential. Specific adsorption of cations is typically associated with a certain degree of electron transfer from the electrode to the cation: [44, 57]

$$C_{aq}^{z+} + * + \delta e^- \rightleftharpoons {}^*C^{(z-\delta)+}, \tag{1}$$

where C is the cation and z is its charge. δe^- describes the partial electron transfer upon specific adsorption on a surface site, denoted with *. In the case of methyl$_4$N$^+$, specific adsorption is therefore expected to reduce the amount of positive charge on the cation by an amount δe^-. In the following, we denote specifically adsorbed cations without a formal charge, but it is important to remember that they retain a significant fraction of their positive charge in the adsorbed state. We hypothesized that partial electron transfer to methyl$_4$N$^+$ upon specific adsorption may red-shift the CH_3 deformation mode.

To test if and to what extent the peak frequency of ν_{as} is affected by the charge on the cation, we employed structurally related model compounds whose charge can be readily changed through their acid-base chemistry: Trimethylamine and its protonated form, trimethylammonium. We emphasize that we explicitly do not imply the conversion of methyl$_4$N$^+$ into either of the two species upon adsorption. Methyl$_4$N$^+$ is stable within the employed potential range, as demonstrated in a recent study. [58] The high degree of reversibility of the spectra during the forward and reverse potential scans (Supplementary Figure 1) also speak against the occurrence of irreversible chemical processes involving methyl$_4$N$^+$. Rather, we utilized these two model molecules to illustrate the relationship between charge on the molecule and the peak frequency of the CH_3 deformation band. Figure 3 shows the spectra of trimethylamine and its protonated form, trimethylammonium, in their bulk solutions. Comparison of the two spectra shows that the peak frequency of the CH_3 deformation band shifts to the red by about $\sim$12 cm^{-1} upon removal of the positive charge from the molecule. On the basis of this observation, we attribute the negative-going band at $\sim$1482 cm^{-1} to methyl$_4$N$_{ads}$ whose positive charge is partially reduced according to Equation 1.

To further corroborate this interpretation, we carried out vibrational frequency and Bader charge analyses on DFT models of methyl$_4$N$^+$ in the gas phase and adsorbed on an Au(111) surface. Computational details are provided in Supplementary Note 1. Consistent with our experimental findings, the DFT models predict a red-shift of the vibrational modes in the range 1400-1480 cm^{-1} by 18-21 cm^{-1} upon adsorption (Supplementary Table 1 and Supplementary Figure 3). Bader charge analysis shows that adsorption of methyl$_4$N$^+$ results in a decrease of the cation's charge from +1.00 to +0.72 due to partial electron transfer from the electrode to the cation (Equation 1, Supplementary Table 2).

Taken together, our experimental observations and computational results indicate that the negative-going band at $\sim$1482 cm^{-1} is attributable to methyl$_4$N$_{ads}$, whose positive charge is less than unity. We note that the distinct dielectric environment at the interface [6, 33] is likely an additional factor that contributes to the observed red-shift of methyl$_4$N$_{ads}$.

Infrared probe of specific alkali metal cation adsorption. The loss of absorbance at $\sim$1482 cm^{-1} as the potential is scanned negatively in the presence of alkali metal cations (Figure 1B, C) could have two possible origins: A potential-induced re-orientation of methyl$_4$N$_{ads}$ that tilts the transition dipole

moment of ν_{as} away from the surface normal or a displacement of $methyl_4N_{ads}$ by specifically adsorbed K^+ (K_{ads}) with decreasing potential. A re-orientation of $methyl_4N_{ads}$ with applied potential is expected around the potential of zero charge. [59] In this study, the employed potential range is significantly negative of the potential of zero charge of polycrystalline Au (PZC = 0.16 V versus the standard hydrogen electrode [60]). Therefore, a potential-induced re-orientation is unlikely to occur in the potential range employed in this work. The second interpretation, namely the displacement of $methyl_4N_{ads}$ by K_{ads}, implies the presence of $methyl_4N_{ads}$ at the reference potential. To test if $methyl_4N_{ads}$ is present at +0.2 V, we collected interfacial spectra at a fixed applied potential by changing the polarization of the IR probe light. In this collection mode, the spectrum collected with s-polarized light serves as the reference and the spectrum collected with p-polarized light as the sample spectrum. Because of the spectroscopic selection rule at metallic interfaces, only the spectrum recorded with p-polarized light contains bands due to interfacial species. [61] As shown in Supplementary Figure 4, the spectrum exhibits an absorbance at $\sim$1482 cm^{-1}, suggesting the presence of $methyl_4N_{ads}$ at +0.2 V. On the basis of this observation and the results presented in Figure 1, the displacement of $methyl_4N_{ads}$ by K_{ads} is a plausible scenario. In the following, we first discuss the physical basis of this scenario and then present additional experimental data in support of this interpretation.

To understand the physical origin of the displacement of $methyl_4N_{ads}$ by K_{ads} at sufficiently cathodic potentials, we examined the potential-dependent adsorption of the cations on Au(111) with DFT. Details of the computational models and methods of analysis are given in Supplementary Note 1. We note that absolute adsorption potentials are highly sensitive to solvation effects, which are challenging to model across different cations. A discussion of solvation effects on adsorption potentials is provided in Supplementary Note 2 and Supplementary Table 3. Here, we focus on trends in the electrosorption valency, which is a measure of the effective number of electrons transferred upon cation adsorption. Within the model, the rate at which the adsorption free energy becomes more negative with decreasing potential is given by the electrosorption valency of the adsorbed cation, that is, the effective number of electrons transferred upon adsorption (δe^- in Equation 1). We calculated the electrosorption valency for the series of alkali metal cations and for $methyl_4N^+$ (Supplementary Table 4). The optimized geometries of the cations adsorbed on the Au(111) are shown in Supplementary Figure 5 and the coordinates of the DFT models are provided as supplementary data. The electrosorption valency for K^+ is larger (0.64) than that of $methyl_4N^+$ (0.51). Therefore, specific adsorption of K^+ becomes more favorable relative to specific adsorption of $methyl_4N^+$ as the potential is tuned negatively. On the basis of these findings, we suggest the difference in electrosorption valencies as the physical origin of the experimentally observed potential-dependent displacement.

The case for specific adsorption of K^+ is also supported by the observation that the desorption of $methyl_4N_{ads}$ represents an oxidation process (the reverse

of Equation 1). For this process to become more favorable with decreasing potential, it logically must be accompanied by a reductive process. Our calculated electrosorption valencies indicate that alkali metal cations can accept electronic charge upon adsorption at the relevant potentials (Supplementary Tables 3 and 4). The fact that the alkali electrosorption valencies are larger than that for $methyl_4N_{ads}$ leads to the conclusion that the adsorbed cation exchange reaction is a reductive process. Therefore, there is a clear physical rationale for an exchange reaction of the form

$$methyl_4N_{ads} + M^+_{aq} + \delta e^- \rightarrow methyl_4N^+_{aq} + M_{ads}, \quad (2)$$

where M^+_{aq} and M_{ads} represent an alkali metal cation in solution and in the adsorbed state, respectively. Figure 1D shows an illustration of our interpretation of the observed potential-induced changes.

To further support the notion of the displacement of $methyl_4N_{ads}$ by K_{ads}, we probed the effects of K^+ addition to a 100 mM $methyl_4N(HCO_3)$ electrolyte while maintaining an electrode potential of −0.45 V (Figure 4). Specifically, we added small aliquots of 2 M $KHCO_3$ to the working electrode compartment to achieve K^+ concentrations in the electrolyte of 10, 30, and 50 mM. The single-beam sample spectra were collected at −0.45 V in the electrolyte composition as indicated in the legend of Figure 4; the single-beam reference spectrum was that of the interface at +0.2 V in 100 mM $methyl_4N^+$ in the absence of K^+ in all cases. In the absence of K^+, only the positive-going peak at ∼1490 cm^{-1} of hydrated $methyl_4N^+$ is present. Akin to the trends observed in Figure 1, sequential additions of K^+ bring about the negative-going band at ∼1482 cm^{-1}, accompanied by a decrease in the amplitude of the band at ∼1490 cm^{-1}. Supplementary Figure 6 demonstrates the reproducibility of the results. These experiments demonstrate that the displacement of $methyl_4N_{ads}$ by K_{ads} is responsible for the negative-going band. Therefore, the band at ∼1482 cm^{-1} is a spectroscopic measure of the coverage of K_{ads}.

Dependence of specific adsorption on hydration free energy. Having established the band at ∼1482 cm^{-1} as a spectroscopic measure of the relative coverage of specifically adsorbed alkali metal cations, we explored to what extent this surface coverage is dependent on the identity of the alkali metal cation. To this end, we conducted experiments as the one shown in Figure 4 with Li^+, Na^+, and Cs^+ (Supplementary Figure 7). The integrated areas of the two bands were determined by fitting a sum of two Gaussian functions and a linear background to the spectra. Details of the fitting procedures and representative fits are provided in the Methods and Supplementary Figure 8. The integrated area the ∼1490 cm^{-1} band monotonically decreases with increasing alkali metal cation concentration (Supplementary Figure 9). Here, we focus on the ∼1482 cm^{-1} band, which quantifies the coverage of specifically adsorbed alkali metal cations. Figure 5 shows the integrated area of the ∼1482 cm^{-1} band, a measure of the coverage of specifically adsorbed alkali metal cations, as a function of bulk alkali metal cation concentration. Clearly, the surface coverage is strongly dependent on the identity of the alkali

metal cation, increasing in the order $Li^+ < Na^+ < K^+ < Cs^+$. Interestingly, the experimentally observed alkali metal cation adsorption trend (Figure 5) is counter to the calculated trend in electrosorption valency (Supplementary Table 4), suggesting that a larger extent of electron transfer upon adsorption (δe^-) does not dictate the relative alkali metal cation adsorption at −0.45 V. This observation suggests that other factors determine the experimentally observed trend. Indeed, the degree to which alkali metal cations displace $methyl_4N_{ads}$ correlates with their experimental free energies of hydration (Figure 6). This observation indicates that alkali metal cations with softer hydration shells have a higher tendency to specifically adsorb on the electrode surface. Because specific alkali metal cation adsorption necessitates partial dehydration, the observed correlation provides further support of a displacement reaction (Equation 2).

Effect of specific cation adsorption on CO_2 reduction. To explore the effects of the coverage of specifically adsorbed alkali metal cations on electrocatalysis, we monitored the rates of CO and H_2 formation during the reduction of CO_2 on polycrystalline Au in the presence of different alkali metal cations. Electrolysis was carried out with an electrochemically roughened Au foil in an H-cell under stirring of the CO_2-saturated electrolyte and an electrode potential of −0.45 V. At this potential, the rate of CO_2 reduction is limited by the adsorption of CO_2 (and not by mass transport). [62–65] The electrolytes contained 100 mM $methyl_4N^+$ and 30 mM of the desired alkali metal cation. Products were detected with gas chromatography. Representative electrochemical current densities and average Faradaic efficiencies are provided in Supplementary Figures 10 and 11, respectively. Figure 7 shows the partial current densities of CO and H_2 as a function of the integrated area of the band at ∼1482 cm^{-1}, a measure of the coverage of specifically adsorbed alkali metal cations. The magnitude of the CO partial current monotonically increases with the tendency of the alkali metal cation to specifically adsorb on the electrode surface (Figure 7A). This observation suggests that the propensity of an alkali metal cation to specifically adsorb on an electrode is a key factor that determines its efficacy in promoting the CO_2 reduction reaction.

The mechanism of alkali metal cation promotion of the CO_2 reduction reaction is beyond the scope of this study. At least two possible mechanisms exist: First, $methyl_4N_{ads}$ may block active sites. [57] Upon displacement of $methyl_4N_{ads}$ by M_{ads}, the blocking effect may be removed. Second, $methyl_4N_{ads}$ may not have any effect on CO_2 reduction. Upon displacement of $methyl_4N_{ads}$ by M_{ads}, the reaction is activated by M_{ads}-intermediate interactions. It is probable that both mechanisms contribute. Prior studies demonstrated that the rate-determining step in CO_2-to-CO conversion is the adsorption of CO_2, which is accompanied by the transfer of an electron. [62–64] It has been suggested that alkali metal cations at the surface stabilize adsorbed CO_2 and the transition state leading to this intermediate. [32] The mechanism of stabilization could be due to favorable electrostatic interactions and/or cations coordinating to the nucleophilic oxygens of adsorbed CO_2. [32, 66]

At the employed electrode potential of −0.45 V, the hydrogen evolution reaction (HER) appears relatively insensitive to the identity of the cation (Figure 7B). However, the rate of the HER is comparatively fast in Li^+- and Na^+-containing electrolytes. We speculate that due to the suppression of the CO_2 reduction reaction in the presence of these cations, a larger fraction of the protons at the interface is available for the HER. Related arguments invoking the competition of two parallel reactions for interfacial protons were presented by others in prior studies. [67–69]

3 Conclusions

In summary, we established an organic cation ($methyl_4N^+$) as an infrared spectroscopic probe of the relative coverages of specifically adsorbed alkali metal cations under electrocatalytic conditions. By probing the ν_{as} of $methyl_4N^+$ at a polycrystalline Au electrode during the reduction of CO_2 to CO, we identified two spectroscopically distinguishable sub-populations of this cation in the EDL: hydrated $methyl_4N^+$ and $methyl_4N_{ads}$. We found that the latter population is displaced by alkali metal cations at catalytically relevant electrode potentials. As a result, ν_{as} of $methyl_4N_{ads}$ is an operando probe of the coverage of specifically adsorbed alkali metal cations. This conclusion is based on three pieces of circumstantial evidence that, when viewed together, provide strong support for specific alkali metal cation adsorption leading to the observed displacement of specifically adsorbed $methyl_4N_{ads}$ species. These three pieces of circumstantial evidence include the correlation between the degree of displacement of $methyl_4N_{ads}$ and the free energy of hydration of the alkali metal cations, the monotonic dependence of the rate of CO formation on the alkali metal cation's propensity to displace $methyl_4N_{ads}$, and the DFT calculations indicating that specific adsorption of alkali metal cations is possible at the experimentally relevant potentials. Importantly, specific alkali metal cation adsorption provides a clear physical rationale for our experimental observations. We determined that the relative surface coverages of different alkali metal cations at the same bulk concentration is determined by their free energy of hydration. Our study indicates that the degree to which alkali metal cations undergo partial dehydration at the electrode surface is key to their ability to promote the reduction of CO_2.

4 Methods

Materials. For electrochemical measurements, Na_2CO_3 (99.997%, Puratronic, trace metals basis), K_2CO_3 (99.997%, Puratronic, trace metals basis), Cs_2CO_3 (99.994%, Puratronic, trace metals basis), tetramethylammonium hydroxide (25 wt % solution in water; 99.9999% trace metals basis), and Au foil (>99.9975%; metals basis, 0.1 mm thick) were acquired from Alfa Aesar. Li_2CO_3 (99.999%, trace metals basis) was aquired from Acros Organics. Graphite rods (3 mm diameter, 99.995% trace metals basis) and $Na_2EDTA{\cdot}2H_2O$ (electrophoresis grade) were obtained from Sigma Aldrich.

High-purity water derived from a Barnstead Nanopure Diamond System was used for electrolyte preparation. CO_2 (research grade) and Ar (ultra high purity) were procured from Air Gas. For electroless deposition of Au films on Si, $Na_2S_2O_3{\cdot}H_2O$ (99.999%; trace metals basis), Na_2SO_3 (98.5%; anhydrous), HF (48 wt %), NH_4F (40 wt %), and $NaAu_4{\cdot}2H_2O$ (99.99%; metals basis) were acquired from Fisher Scientific (Waltham, MA). Polycrystalline diamond pastes were purchased from Ted Pella (Redding, CA).

Electrolyte Preparation. Electrolytes for all experiments were prepared by dissolving the appropriate combination of tetramethylammonium and alkali metal cation salts to reach the desired cation concentration. With the exception of experiments in Figures 1 and 2, all electrolytes contained 10 μM ethylenediamine-tetra-acetic acid (EDTA) to prevent unwanted electrodeposition of metal ion impurities onto the Au electrode surface.[70–72] The electrolyte was then purged with CO_2 at 40 standard cubic centimeters per minute (sccm) for 2 hours or until the electrolyte pH reached a stable reading of 6.8±0.1.

SEIRAS. SEIRAS experiments were carried out in a home-built two-compartment poly-etheretherketone (PEEK) cell with the catholyte (6 ml) and anolyte (5 ml) separated by a Selemion AMV anion exchange membrane (AGC Engineering Co.; Chiba, Japan). A detailed description of the SEIRAS cell was provided previously. [73] The Au thin-film electrode was deposited onto a Si ATR prism as described previously. [74] Following the Au film deposition, the surface was rinsed with high purity water, blow-dried with N_2 gas, and assembled into the electrochemical cell. A graphite rod and an Ag/AgCl electrode (3 M NaCl; Basi Inc.; West Lafayette, IN) were used as the counter and reference electrodes, respectively. Under stirring at 900 rotations per minute (rpm) with a magnetic stir bar and the cell at open circuit, the catholyte was first purged with CO_2 at 10 sccm for 20 min. The potential was stepped to −1.3 V versus Ag/AgCl and held for 60 s to activate the Au film.[75] Then, the potential was held at +0.2 V versus RHE for 10 min while the catholyte was stirred at 900 rpm and purged with CO_2 at 10 sccm. Within the final minute of this 10 min period, 10 single-beam spectra were averaged to use as the single-beam reference spectrum. Without returning to open circuit, the electrode potential was then altered according to the experiment of interest while single-beam sample spectra were recorded, with the CO_2 purging rate and stirring rate maintained for the duration of the experiment. For alkali metal cation addition experiments (Figure 5), the potential was alternately stepped between +0.2 and −0.45 V in 1 min intervals. The single-beam sample spectrum was taken at ∼30 s after stepping the potential to −0.45 V. The aliquots of alkali cation stock solution were added in the intervals right after returning to +0.2 V. Single-beam spectra were used to calculate the difference spectra shown in the respective figures ($\Delta\text{mOD} = -10^3 \log_{10} \frac{S}{R}$). Spectra were collected with a 40 kHz scanner velocity, a 4 cm^{-1} spectral resolution, and 4.6 s temporal resolution. The cell was connected to a nitrogen-purged ATR accessory (VeeMax III; Pike Technologies; Madison, WI) in the sample compartment of a Bruker Vertex 70

Fourier-transform infrared (FTIR) spectrometer, which was interfaced with a liquid nitrogen-cooled mercury cadmium telluride (MCT) detector (FTIR-16; Infrared Associates; Stuart, FL). The electrode potential was controlled with a VSP-300 potentiostat (Biologic; Seyssinet-Pariset, France). 85% of the solution resistance was compensated *in situ*. The remaining 15% was manually corrected following each experiment. For alkali cation addition experiments, compensation of the solution resistance (85%) was readjusted after each addition of alkali cation solution to account for the increase in conductivity in the electrolyte.

Peak Fitting Procedure. For determination of the integrated band areas shown in Figure 5 and Supplementary Figure 9, a combination of a linear background and two Gaussian functions were fit to the spectra. The peak positions and widths of the Gaussians describing the negative-going and positive-going bands at 1482 cm^{-1} and ∼1490 cm^{-1} were first determined as follows: For the peak at ∼1490 cm^{-1}, the best fit was determined for a 100 mM $methyl_4N(HCO_3)$ electrolyte in the absence of alkali metal cations where no negative-going band is present (Supplementary Figure 8A). For the peak at ∼1482 cm^{-1}, the best fit was determined in the 50 mM $methyl_4N(HCO_3)$ and 50 mM $KHCO_3$ mixture, where no significant positive peak was present (Supplementary Figure 8B). To find the optimum fit for the biphasic spectra, the extracted peak positions and widths were kept constant and only the band amplitudes of the two Gaussian functions were used as fitting parameters (Supplementary Figure 8C).

Product Detection. Product detection was carried out in a two-compartment custom glass cell (Adams & Chittenden; Berkeley, CA). The catholyte and anolyte compartments contained 8.5 mL and 9.5 mL of electrolyte, respectively, and were separated by a Selemion AMV anion exchange membrane (AGC Engineering Co.; Chiba, Japan). To clean the Au foil, the surface was treated with aqua regia for 30 s, rinsed plentifully with high purity water, and blow-dried with N_2 gas. The Au working electrode with an exposed geometric surface area of 1.0 cm^2 was then introduced into the solution. The Au electrode was first anodically roughened. This procedure involved cycling the potential between −0.6 and 2.3 V at 50 mVs^{-1} in CO_2-saturated 0.1 M $KHCO_3$ electrolyte for three cycles, with a potential hold at 2.3 V for 30 min after the first cycle. [76] Immediately following the roughening procedure, the potential was stepped to −0.45 V for 30 min to reduce the Au surface. The electrode was then rinsed with high purity water and introduced into a clean cell with a fresh membrane and the electrolyte of interest.

The catholyte was stirred with a magnetic stir bar at 900 rpm throughout the experiments. Prior to the start of electrolysis, the catholyte was purged with CO_2 at 10 sccm for 20 min. The CO_2 purge was continued throughout the experiment. The potential was then stepped to −0.45 V and a sample of the head space of the cathode compartment was taken after the first 10 min of electrolysis and analyzed with gas chromatography (GC). An SRI Instruments (Torrance, CA) Mulit-Gas 5 Configuration gas chromatograph

was calibrated with a gas mixture containing CO and H_2. A thermal conductivity detector (TCD) and a flame ionization detector (FID) were used to measure the produced amounts of H_2 and CO, respectively. The partial current density for each product was calculated according to: partial current = gas product volume% $\times$ flow rate $\times \frac{nFP}{RT} \times \frac{1}{A}$, where the gas product volume% is determined from the calibrated GC measurement, the flow rate is in liters per second, P = 101,325 Pa, T = 295.15 K, and A is the geometric surface area of the electrode. For the calculation of Faradaic efficiences, the total current was averaged over a 30 s time-segment at the moment the gas sample was taken. The potential was controlled with a Versastat 3 potentiostat (AMETEK, Berwyn, PA). 85% of the solution resistance was compensated in situ. The remaining 15% was manually corrected after the experiment.

Spectra of Species in Bulk Solution. The spectra of the CH_3 deformation band of species in bulk solution were collected with a Horizon Multiple Reflection ATR Accessory (Harrick Scientific, Pleasantville, NY) equipped with a ZnSe crystal.

5 Data Availability

Representative data and extended datasets that support the findings reported in this study are available in the manuscript and the Supplementary Information. The data of the figures shown in the main text and the DFT-calculated coordinates for the optimized geometries of the cations on Au(111) are provided in machine-readable formats as supplementary files. Additional data are available from the corresponding authors upon reasonable request.

6 Acknowledgements

This work was supported by a CAREER award (to M.M.W.) from the National Science Foundation (Award No.: CHE-1847841). N.A. and M.J.J. acknowledge the National Science Foundation for support (Award No.: CHE-1665155).

7 Author Contributions

All authors discussed the results and commented on and revised the manuscript. M.M.W. and V.J.O. conceived and designed the experiments. V.J.O. conducted the experiments. Y.S.H. participated in data collection. M.J.J. and N.A. contributed the DFT work.

8 Competing Interests

The authors declare no competing interests.

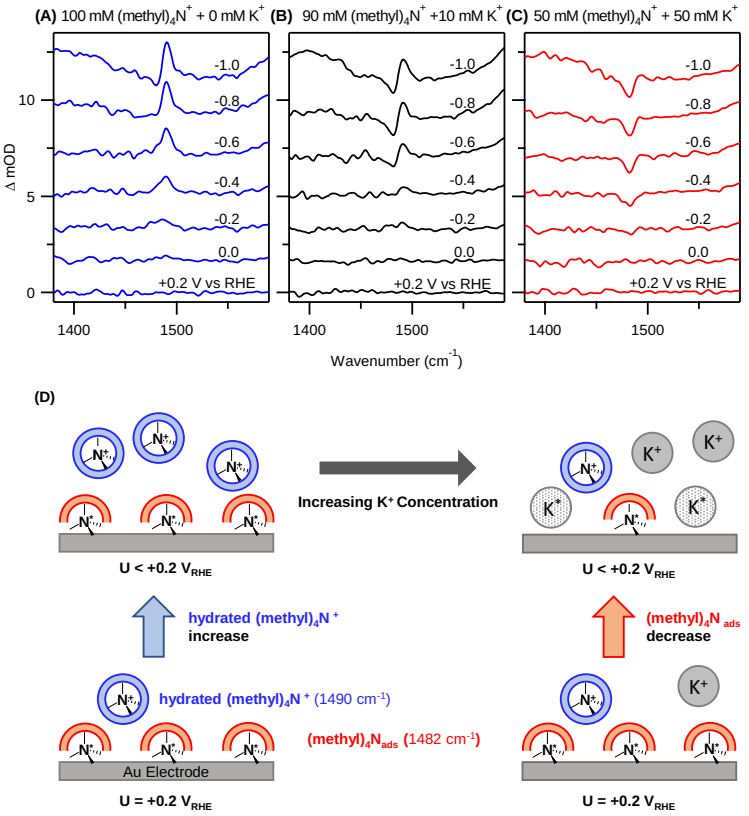

Fig. 1 Response of the CH_3 deformation band of methyl$_4$N$^+$ to changes in EDL structure. Representative potential-dependent spectra of aqueous electrolyte/polycrystalline Au interfaces during cathodic forward scans (scan rate: 2 mV s^{-1}). The CO_2-saturated electrolytes contained (A) 100 mM methyl$_4$N$^+$, (B) 90 mM methyl$_4$N$^+$ and 10 mM K^+, and (C) 50 mM methyl$_4$N$^+$ and 50 mM K^+ with bicarbonate as the common anion. The spectra were collected with SEIRAS-ATR and are vertically offset for clarity. The ordinate represents change in optical density. (D) Schematic illustration of the interpretation of the spectra. In the absence of K^+, hydrated methyl$_4$N$^+$ accumulates in the EDL with decreasing potential, as evidenced by the increase in the ~1490 cm^{-1} band (panel A). In the presence of K^+, methyl$_4$N$_{ads}$ is displaced by K_{ads}, as indicated by the decrease in the ~1482 cm^{-1} band (panel C). K_{ads} is indicated by the grey patterned circles. The hydration shells of the K^+ are not shown for clarity. The blue and red arrows indicate decreasing electrode potential (U).

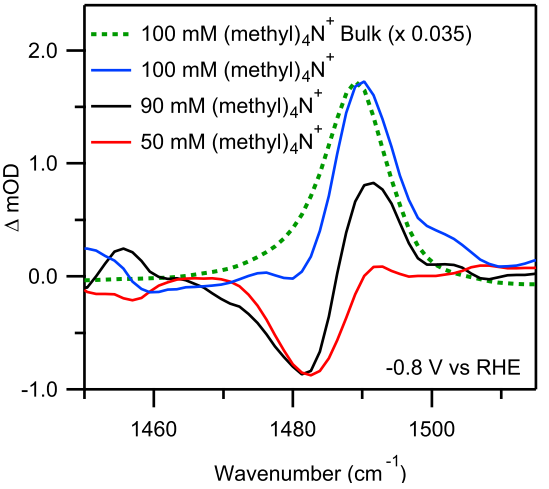

Fig. 2 Comparison of CH_3 deformation bands of methyl$_4$N$^+$ in different electrolytes. Representative spectra of aqueous, CO_2-saturated electrolyte/polycrystalline Au interfaces at an electrode potential of −0.8 V taken with SEIRAS-ATR (solid lines) during the cathodic forward scans shown in Figure 1. The concentrations of methyl$_4$N$^+$ indicated in the legend were balanced by K^+ to a total cation concentration of 100 mM. Bicarbonate was the common anion. The ordinate represents change in optical density. The green dashed line represents the absorbance spectrum of 100 mM of methyl$_4$N$^+$ in bulk solution (bicarbonate), collected on a ZnSe ATR crystal. Deionized water was used as the reference for this spectrum.

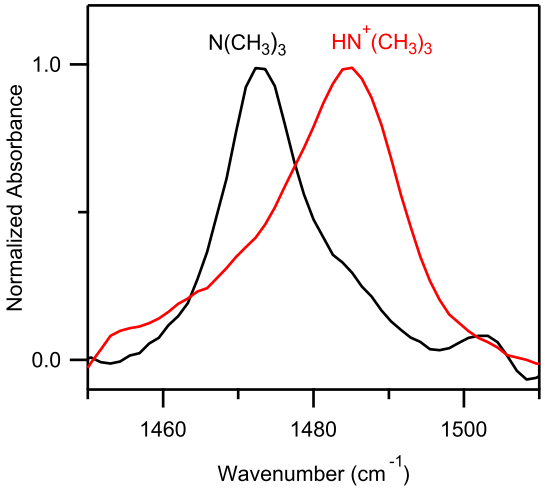

Fig. 3 Dependence of CH_3 deformation band on charge on molecule. Normalized absorbance spectra of trimethylamine (black, 10 mM methyl$_3$N plus 10 mM NaOH) and trimethylammonium (red, 10 mM methyl$_3$N plus 10 mM HCl) in bulk aqueous solutions. The spectra were collected on a ZnSe ATR crystal. The respective acidified/basified solution in the absence of the analyte was used as the reference.

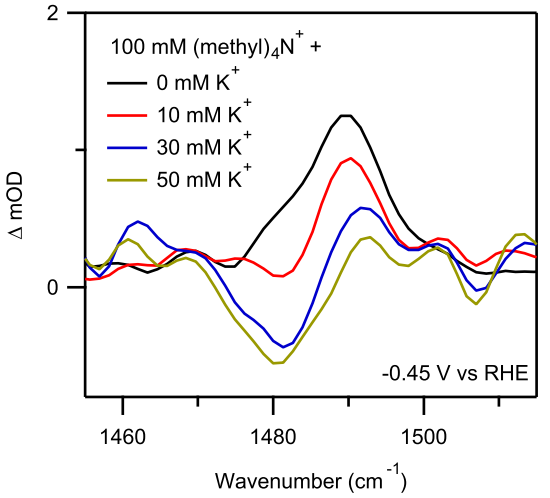

Fig. 4 Response of CH_3 deformation band to addition of K^+ to the electrolyte. Change of lineshape of ν_{as} of methyl$_4N^+$ at the electrolyte/Au interface with addition of K^+ to an electrolyte initially containing only 100 mM methyl$_4$N(HCO_3) (black) at an electrode potential of −0.45 V. Spectra were collected with SEIRAS-ATR. Small aliquots of 2 M $KHCO_3$ were added to achieve the desired concentration of K^+ indicated in the legend.

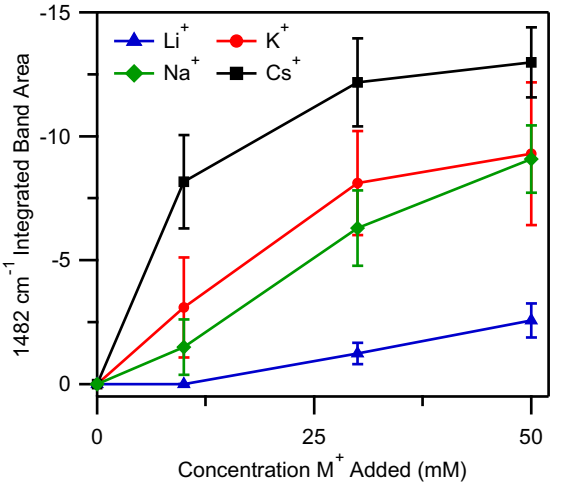

Fig. 5 Change of 1482 cm^{-1} band area with bulk alkali metal cation concentration. Coverage of specifically adsorbed alkali metal cations at −0.45 V as measured by the integrated area of the 1482 cm^{-1} band as a function of alkali metal cation concentration in the bulk. The corresponding spectra were collected with SEIRAS-ATR at the aqueous electrolyte/polycrystalline Au interface. All electrolytes initially contained only 100 mM methyl$_4$N(HCO_3). Small aliquots of the bicarbonate salt of the desired alkali metal cation were added to achieve the desired concentration. Error bars (± 1 standard deviation) were calculated on the basis of at least 3 independent experiments.

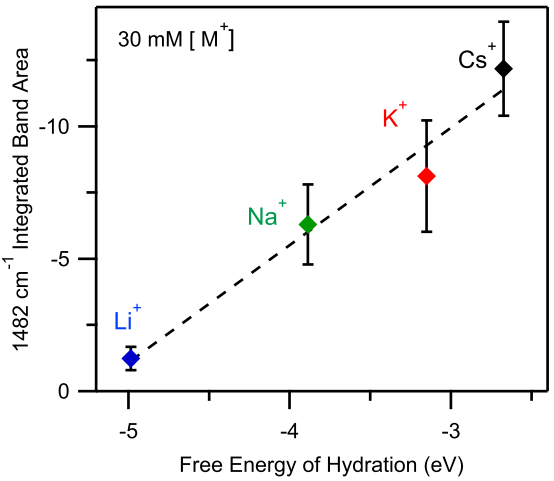

Fig. 6 Correlation between 1482 cm^{-1} band area and alkali cation hydration free energy. Coverage of specifically adsorbed alkali metal cations as measured by the integrated area of the band at ∼1482 cm^{-1} at −0.45 V plotted against experimental cation hydration free energies at 300 K and 1 M taken from reference 77. The bulk concentration of the alkali metal cations was 30 mM. The dashed line is a fit of a linear function to the data points. The error bars (± 1 standard deviation) were calculated on the basis of at least 3 independent experiments.

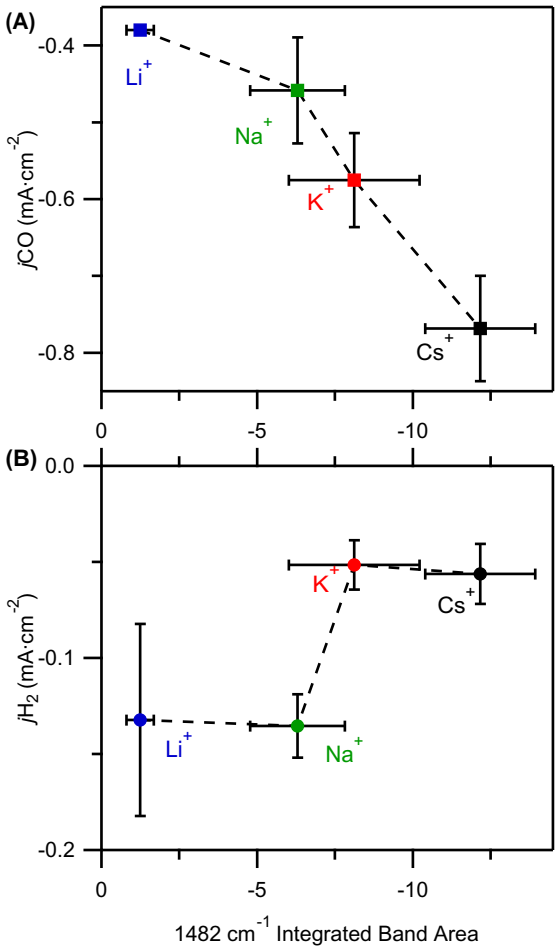

Fig. 7 Dependence of electrocatalysis on 1482 cm^{-1} integrated band area. Geometric partial current densities of (A) CO and (B) H_2 at −0.45 V as a function of coverage of specifically adsorbed alkali metal cations as measured by the integrated area of the band at ∼1482 cm^{-1}. The bulk electrolyte was 100 mM methyl$_4$N$^+$ and 30 mM of the desired alkali metal cation with bicarbonate as the common anion. Electrolysis was carried out in a two-compartment electrochemical cell with an electrochemically roughened Au electrode serving as the working electrode. Products were quantified with gas chromatography after 10 min of electrolysis. Error bars (± 1 standard deviation) were calculated on the basis of at least 3 independent experiments.

References

[1] Parsons, R.: The electrical double layer: Recent experimental and theoretical developments. Chem. Rev. **90**(5), 813–826 (1990) https://doi.org/10.1021/cr00103a008. https://doi.org/10.1021/cr00103a008

[2] Dunwell, M., Yan, Y., Xu, B.: Understanding the influence of the electrochemical double-layer on heterogeneous electrochemical reactions. Curr. Opin. Chem. Eng. **20**, 151–158 (2018). https://doi.org/10.1016/j.coche.2018.05.003

[3] Magnussen, O.M., Groß, A.: Toward an atomic-scale understanding of electrochemical interface structure and dynamics. J. Am. Chem. Soc. **141**(12), 4777–4790 (2019) https://doi.org/10.1021/jacs.8b13188. https://doi.org/10.1021/jacs.8b13188

[4] Waegele, M.M., Gunathunge, C.M., Li, J., Li, X.: How cations affect the electric double layer and the rates and selectivity of electrocatalytic processes. J. Chem. Phys. **151**(16), 160902 (2019) https://doi.org/10.1063/1.5124878. https://doi.org/10.1063/1.5124878

[5] Grahame, D.C.: The electrical double layer and the theory of electrocapillarity. Chem. Rev. **41**(3), 441–501 (1947) https://doi.org/10.1021/cr60130a002. https://doi.org/10.1021/cr60130a002

[6] Sorenson, S.A., Patrow, J.G., Dawlaty, J.M.: Solvation reaction field at the interface measured by vibrational sum frequency generation spectroscopy. J. Am. Chem. Soc. **139**, 2369–2378 (2017) https://doi.org/10.1021/jacs.6b11940. https://doi.org/10.1021/jacs.6b11940

[7] Raberg, J.H., Vatamanu, J., Harris, S.J., van Oversteeg, C.H.M., Ramos, A., Borodin, O., Cuk, T.: Probing electric double-layer composition via in situ vibrational spectroscopy and molecular simulations. J. Phys. Chem. Lett. **10**(12), 3381–3389 (2019). https://doi.org/10.1021/acs.jpclett.9b00879

[8] Zhang, R., Han, M., Ta, K., Madsen, K.E., Chen, X., Zhang, X., Espinosa-Marzal, R.M., Gewirth, A.A.: Potential-dependent layering in the electrochemical double layer of water-in-salt electrolytes. ACS Appl. Energy Mater. **3**(8), 8086–8094 (2020). https://doi.org/10.1021/acsaem.0c01534

[9] Xue, S., Garlyyev, B., Auer, A., Kunze-Liebhäuser, J., Bandarenka, A.S.: How the nature of the alkali metal cations influences the double-layer capacitance of Cu, Au, and Pt single-crystal electrodes. J. Phys. Chem. C

124(23), 12442–12447 (2020). https://doi.org/10.1021/acs.jpcc.0c01715

[10] Zhang, Y., Tang, J., Ni, Z., Zhao, Y., Jia, F., Luo, Q., Mao, L., Zhu, Z., Wang, F.: Real-time characterization of the fine structure and dynamics of an electrical double layer at electrode–electrolyte interfaces. J. Phys. Chem. Lett. **12**(22), 5279–5285 (2021). https://doi.org/10.1021/acs.jpclett.1c01134

[11] Goldsmith, Z.K., Calegari Andrade, M.F., Selloni, A.: Effects of applied voltage on water at a gold electrode interface from ab initio molecular dynamics. Chem. Sci. **12**, 5865–5873 (2021). https://doi.org/10.1039/D1SC00354B

[12] Ojha, K., Doblhoff-Dier, K., Koper, M.T.M.: Double-layer structure of the Pt(111)–aqueous electrolyte interface. Proc. Natl. Acad. Sci. **119**(3), 2116016119 (2022) https://www.pnas.org/doi/pdf/10.1073/pnas.2116016119. https://doi.org/10.1073/pnas.2116016119

[13] Herasymenko, P., Šlendyk, I.: Wasserstoffüberspannung und adsorption der ionen [*Hydrogen overpotential and adsorption of ions.*]. Z. Phys. Chem. A **149**, 123–139 (1930)

[14] Frumkin, A.N.: Influence of cation adsorption on the kinetics of electrode processes. Trans. Faraday Soc. **55**, 156–167 (1959). https://doi.org/10.1039/TF9595500156

[15] Danilovic, N., Subbaraman, R., Strmcnik, D., Paulikas, A.P., Myers, D., Stamenkovic, V.R., Markovic, N.M.: The effect of noncovalent interactions on the HOR, ORR, and HER on Ru, Ir, and $Ru_{0.50}Ir_{0.50}$ metal surfaces in alkaline environments. Electrocatal. **3**, 221–229 (2012). https://doi.org/10.1007/s12678-012-0100-7

[16] Arán-Ais, R.M., Gao, D., Roldan Cuenya, B.: Structure- and electrolyte-sensitivity in CO_2 electroreduction. Acc. Chem. Res. **51**, 2906–2917 (2018) https://doi.org/10.1021/acs.accounts.8b00360. https://doi.org/10.1021/acs.accounts.8b00360

[17] Li, J., Chang, X., Zhang, H., Malkani, A.S., Cheng, M.-j., Xu, B., Lu, Q.: Electrokinetic and in situ spectroscopic investigations of CO electrochemical reduction on copper. Nat. Commun. **12**(1), 3264 (2021). https://doi.org/10.1038/s41467-021-23582-2

[18] Rosca, V., Duca, M., de Groot, M.T., Koper, M.T.M.: Nitrogen cycle electrocatalysis. Chem. Rev. **109**(6), 2209–2244 (2009) https://doi.org/10.1021/cr8003696. https://doi.org/10.1021/cr8003696

[19] McEnaney, J.M., Blair, S.J., Nielander, A.C., Schwalbe, J.A., Koshy, D.M., Cargnello, M., Jaramillo, T.F.: Electrolyte engineering for efficient electrochemical nitrate reduction to ammonia on a titanium electrode. ACS Sustain. Chem. Eng. **8**(7), 2672–2681 (2020). https://doi.org/10.1021/acssuschemeng.9b05983

[20] Yang, X., Wang, Y., Li, C.M., Wang, D.: Mechanisms of water oxidation on heterogeneous catalyst surfaces. Nano Res. **14**(10), 3446–3457 (2021). https://doi.org/10.1007/s12274-021-3607-5

[21] Huang, J., Li, M., Eslamibidgoli, M.J., Eikerling, M., Groß, A.: Cation overcrowding effect on the oxygen evolution reaction. JACS Au **1**(10), 1752–1765 (2021). https://doi.org/10.1021/jacsau.1c00315

[22] Resasco, J., Chen, L.D., Clark, E., Tsai, C., Hahn, C., Jaramillo, T.F., Chan, K., Bell, A.T.: Promoter effects of alkali metal cations on the electrochemical reduction of carbon dioxide. J. Am. Chem. Soc. **139**, 11277–11287 (2017) http://dx.doi.org/10.1021/jacs.7b06765

[23] Rao, R.R., Huang, B., Katayama, Y., Hwang, J., Kawaguchi, T., Lunger, J.R., Peng, J., Zhang, Y., Morinaga, A., Zhou, H., You, H., Shao-Horn, Y.: pH- and cation-dependent water oxidation on rutile RuO_2(110). J. Phys. Chem. C **125**(15), 8195–8207 (2021). https://doi.org/10.1021/acs.jpcc.1c00413

[24] Strmcnik, D., Kodama, K., van der Vliet, D., Greeley, J., Stamenkovic, V.R., Marković, N.M.: The role of non-covalent interactions in electrocatalytic fuel-cell reactions on platinum. Nat. Chem. **1**, 466–472 (2009) http://dx.doi.org/10.1038/nchem.330. https://doi.org/10.1038/nchem.330

[25] Feaster, J.T., Jongerius, A.L., Liu, X., Urushihara, M., Nitopi, S.A., Hahn, C., Chan, K., Nørskov, J.K., Jaramillo, T.F.: Understanding the influence of [EMIM]Cl on the suppression of the hydrogen evolution reaction on transition metal electrodes. Langmuir **33**, 9464–9471 (2017) https://doi.org/10.1021/acs.langmuir.7b01170. https://doi.org/10.1021/acs.langmuir.7b01170

[26] Bhargava, S.S., Cofell, E.R., Chumble, P., Azmoodeh, D., Someshwar, S., Kenis, P.J.A.: Exploring multivalent cations-based electrolytes for CO_2 electroreduction. Electrochim. Acta **394**, 139055 (2021)

[27] Chen, L.D., Urushihara, M., Chan, K., Nørskov, J.K.: Electric field effects in electrochemical CO_2 reduction. ACS Catal. **6**, 7133–7139 (2016) http://dx.doi.org/10.1021/acscatal.6b02299. https://doi.org/10.1021/acscatal.6b02299

[28] Akhade, S.A., McCrum, I.T., Janik, M.J.: The impact of specifically adsorbed ions on the copper-catalyzed electroreduction of CO_2. J. Electrochem. Soc. **163**, 477–484 (2016) http://jes.ecsdl.org/content/163/6/F477.full.pdf+html. https://doi.org/10.1149/2.0581606jes

[29] Gunathunge, C.M., Ovalle, V.J., Waegele, M.M.: Probing promoting effects of alkali cations on the reduction of CO at the aqueous electrolyte/-copper interface. Phys. Chem. Chem. Phys. **19**, 30166–30172 (2017). https://doi.org/10.1039/C7CP06087D

[30] Chen, X., McCrum, I.T., Schwarz, K.A., Janik, M.J., Koper, M.T.M.: Co-adsorption of cations as the cause of the apparent pH dependence of hydrogen adsorption on a stepped platinum single-crystal electrode. Angew. Chem. Int. Ed. **56**(47), 15025–15029 (2017) https://doi.org/10.1002/anie.201709455. https://doi.org/10.1002/anie.201709455

[31] Pérez-Gallent, E., Marcandalli, G., Figueiredo, M.C., Calle-Vallejo, F., Koper, M.T.M.: Structure- and potential-dependent cation effects on CO reduction at copper single-crystal electrodes. J. Am. Chem. Soc. **139**, 16412–16419 (2017) https://doi.org/10.1021/jacs.7b10142. https://doi.org/10.1021/jacs.7b10142

[32] Monteiro, M.C.O., Dattila, F., Hagedoorn, B., García-Muelas, R., López, N., Koper, M.T.M.: Absence of CO_2 electroreduction on copper, gold and silver electrodes without metal cations in solution. Nat. Catal. **4**(8), 654–662 (2021). https://doi.org/10.1038/s41929-021-00655-5

[33] Zhu, Q., Wallentine, S.K., Deng, G.-H., Rebstock, J.A., Baker, L.R.: The solvation-induced onsager reaction field rather than the double-layer field controls CO_2 reduction on gold. JACS Au **2**(2), 472–482 (2022). https://doi.org/10.1021/jacsau.1c00512

[34] Liu, H., Liu, J., Yang, B.: Promotional role of a cation intermediate complex in C_2 formation from electrochemical reduction of CO_2 over cu. ACS Catal. **11**(19), 12336–12343 (2021). https://doi.org/10.1021/acscatal.1c01072

[35] Fink, A.G., Lees, E.W., Zhang, Z., Ren, S., Delima, R.S., Berlinguette, C.P.: Impact of alkali cation identity on the conversion of HCO_3^- to CO in bicarbonate electrolyzers. ChemElectroChem **8**(11), 2094–2100 (2021). https://doi.org/10.1002/celc.202100408

[36] Singh, M.R., Kwon, Y., Lum, Y., Ager, J.W., Bell, A.T.: Hydrolysis of electrolyte cations enhances the electrochemical reduction of CO_2 over Ag and Cu. J. Am. Chem. Soc. **138**, 13006–13012

(2016) http://dx.doi.org/10.1021/jacs.6b07612. https://doi.org/10.1021/jacs.6b07612

[37] Ayemoba, O., Cuesta, A.: Spectroscopic evidence of size-dependent buffering of interfacial pH by cation hydrolysis during CO_2 electroreduction. ACS Appl. Mater. Interfaces **9**, 27377–27382 (2017) http://dx.doi.org/10.1021/acsami.7b07351. https://doi.org/10.1021/acsami.7b07351

[38] Zhang, F., Co, A.C.: Direct evidence of local pH change and the role of alkali cation during CO_2 electroreduction in aqueous media. Angew. Chem. Inter. Ed. **58**, 2–10 (2019). https://doi.org/10.1002/anie.201912637

[39] Li, J., Li, X., Gunathunge, C.M., Waegele, M.M.: Hydrogen bonding steers the product selectivity of electrocatalytic CO reduction. Proc. Natl. Acad. Sci. U.S.A. **116**(19), 9220–9229 (2019) https://www.pnas.org/content/116/19/9220.full.pdf. https://doi.org/10.1073/pnas.1900761116

[40] Zhang, Z.-Q., Banerjee, S., Thoi, V.S., Shoji Hall, A.: Reorganization of interfacial water by an amphiphilic cationic surfactant promotes CO_2 reduction. J. Phys. Chem. Lett. **11**(14), 5457–5463 (2020). https://doi.org/10.1021/acs.jpclett.0c01334

[41] Hussain, G., Pérez-Martínez, L., Le, J.-B., Papasizza, M., Cabello, G., Cheng, J., Cuesta, A.: How cations determine the interfacial potential profile: Relevance for the CO_2 reduction reaction. Electrochim. Acta **327**, 135055 (2019)

[42] Malkani, A.S., Li, J., Oliveira, N.J., He, M., Chang, X., Xu, B., Lu, Q.: Understanding the electric and nonelectric field components of the cation effect on the electrochemical CO reduction reaction. Sci. Adv. **6**(45), 2569 (2020). https://doi.org/10.1126/sciadv.abd2569

[43] Wallentine, S., Bandaranayake, S., Biswas, S., Baker, L.R.: Direct observation of carbon dioxide electroreduction on gold: Site blocking by the stern layer controls CO_2 adsorption kinetics. J. Phys. Chem. Lett. **11**(19), 8307–8313 (2020). https://doi.org/10.1021/acs.jpclett.0c02628

[44] Mills, J.N., McCrum, I.T., Janik, M.J.: Alkali cation specific adsorption onto fcc(111) transition metal electrodes. Phys. Chem. Chem. Phys. **16**, 13699–13707 (2014). https://doi.org/10.1039/C4CP00760C

[45] Matanovic, I., Atanassov, P., Garzon, F., Henson, N.J.: Density functional theory study of the alkali metal cation adsorption on Pt(111), Pt(100), and Pt(110) surfaces. ECS Trans. **61**(13), 47–53 (2014). https://doi.org/

10.1149/06113.0047ecst

[46] McCrum, I.T., Janik, M.J.: pH and alkali cation effects on the Pt cyclic voltammogram explained using density functional theory. J. Phys. Chem. C **120**(1), 457–471 (2016). https://doi.org/10.1021/acs.jpcc.5b10979

[47] Frank, D.G., Katekaru, J.Y., Rosasco, S.D., Salaita, G.N., Schardt, B.C., Soriaga, M.P., Stern, D.A., Stickney, J.L., Hubbard, A.T.: pH and potential dependence of the electrical double layer at well-defined electrode surfaces: Cs^+ and Ca^{2+} ions at Pt(111) $(2\sqrt{3} \times 2\sqrt{3})$R30°-CN, Pt(111) $(\sqrt{13} \times \sqrt{13})$R14°-CN, and Pt(111) (2×2)-SCN. Langmuir **1**(5), 587–592 (1985) https://doi.org/10.1021/la00065a013. https://doi.org/10.1021/la00065a013

[48] Salaita, G.N., Stern, D.A., Lu, F., Baltruschat, H., Schardt, B.C., Stickney, J.L., Soriaga, M.P., Frank, D.G., Hubbard, A.T.: Structure and composition of a platinum(111) surface as a function of pH and electrode potential in aqueous bromide solutions. Langmuir **2**(6), 828–835 (1986) https://doi.org/10.1021/la00072a031. https://doi.org/10.1021/la00072a031

[49] Lucas, C.A., Thompson, P., Gründer, Y., Markovic, N.M.: The structure of the electrochemical double layer: Ag(111) in alkaline electrolyte. Electrochem. Commun. **13**(11), 1205–1208 (2011)

[50] Strmcnik, D., van der Vliet, D.F., Chang, K.-C., Komanicky, V., Kodama, K., You, H., Stamenkovic, V.R., Marković, N.M.: Effects of Li^+, K^+, and Ba^{2+} cations on the ORR at model and high surface area Pt and Au surfaces in alkaline solutions. J. Phys. Chem. Lett. **2**, 2733–2736 (2011) https://doi.org/10.1021/jz201215u. https://doi.org/10.1021/jz201215u

[51] Liu, Y., Kawaguchi, T., Pierce, M.S., Komanicky, V., You, H.: Layering and ordering in electrochemical double layers. J. Phys. Chem. Lett. **9**(6), 1265–1271 (2018). https://doi.org/10.1021/acs.jpclett.8b00123

[52] Kawaguchi, T., Liu, Y., Karapetrova, E.A., Komanicky, V., You, H.: *In-Situ* to *Ex-Situ* in-plane structure evolution of stern layers on Pt(111) surface: Surface x-ray scattering studies. J. Electroanal. Chem. **875**, 114495 (2020)

[53] Sarkar, S., Maitra, A., Banerjee, S., Thoi, V.S., Dawlaty, J.M.: Electric fields at metal–surfactant interfaces: A combined vibrational spectroscopy and capacitance study. J. Phys. Chem. B **124**(7), 1311–1321 (2020). https://doi.org/10.1021/acs.jpcb.0c00560

[54] Pennathur, A.K., Voegtle, M.J., Menachekanian, S., Dawlaty, J.M.:

Strong propensity of ionic liquids in their aqueous solutions for an organic-modified metal surface. J. Phys. Chem. C **124**(34), 7500–7507 (2020). https://doi.org/10.1021/acs.jpcb.0c04665

[55] Voegtle, M.J., Pal, T., Pennathur, A.K., Menachekanian, S., Patrow, J.G., Sarkar, S., Cui, Q., Dawlaty, J.M.: Interfacial polarization and ionic structure at the ionic liquid–metal interface studied by vibrational spectroscopy and molecular dynamics simulations. J. Phys. Chem. C **125**(10), 2741–2753 (2021). https://doi.org/10.1021/acs.jpcb.0c11232

[56] Harmon, K.M., Gennick, I., Madeira, S.L.: Hydrogen bonding. iv. correlation of infrared spectral properties with C-H$\cdots$X hydrogen bonding and crystal habit in tetramethylammonium ion salts. J. Phys. Chem. **78**(25), 2585–2591 (1974). https://doi.org/10.1021/j100618a012

[57] McCrum, I.T., Hickner, M.A., Janik, M.J.: Quaternary ammonium cation specific adsorption on platinum electrodes: A combined experimental and density functional theory study. J. Electrochem. Soc. **165**, 114–121 (2018). https://doi.org/10.1149/2.1351802jes

[58] He, F., Chen, W., Zhu, B.-Q., Zhen, E.-f., Cai, J., Chen, Y.-X.: Stability of quaternary akyl ammonium cations during the hydrogen evolution reduction: A differential electrochemical mass spectrometry study. J. Phys. Chem. C **125**(10), 5715–5722 (2021). https://doi.org/10.1021/acs.jpcc.1c00960

[59] Deng, Z., Irish, D.E.: Potential dependence of the orientation of $(CH_3)_4N^+$ adsorbed on a silver electrode. a SERS investigation. J. Phys. Chem. **98**(38), 9371–9373 (1994). https://doi.org/10.1021/j100089a001

[60] Trasatti, S., Lust, E.: Modern Aspects of Electrochemistry, p. 78. KluwerAcademic/PlenumPublishers, New York (1999). Chap. The Potential of Zero Charge

[61] Osawa, M.: Dynamic processes in electrochemical reactions studied by surface-enhanced infrared absorption spectroscopy (SEIRAS). B. Chem. Soc. Jpn. **70**(12), 2861–2880 (1997) https://doi.org/10.1246/bcsj.70.2861. https://doi.org/10.1246/bcsj.70.2861

[62] Wuttig, A., Yaguchi, M., Motobayashi, K., Osawa, M., Surendranath, Y.: Inhibited proton transfer enhances Au-catalyzed CO_2-to-fuels selectivity. Proc. Natl. Acad. Sci. U.S.A. **113**(32), 4585–4593 (2016) http://www.pnas.org/content/113/32/E4585.full.pdf. https://doi.org/10.1073/pnas.1602984113

[63] Dong, Q., Zhang, X., He, D., Lang, C., Wang, D.: Role of H_2O in CO_2 electrochemical reduction as studied in a water-in-salt system. ACS Cent.

Sci. **5**(8), 1461–1467 (2019). https://doi.org/10.1021/acscentsci.9b00519

[64] Zhang, B.A., Ozel, T., Elias, J.S., Costentin, C., Nocera, D.G.: Interplay of homogeneous reactions, mass transport, and kinetics in determining selectivity of the reduction of CO_2 on gold electrodes. ACS Cent. Sci. **5**(6), 1097–1105 (2019). https://doi.org/10.1021/acscentsci.9b00302

[65] Ringe, S., Morales-Guio, C.G., Chen, L.D., Fields, M., Jaramillo, T.F., Hahn, C., Chan, K.: Double layer charging driven carbon dioxide adsorption limits the rate of electrochemical carbon dioxide reduction on gold. Nat. Commun. **11**(1), 33 (2020). https://doi.org/10.1038/s41467-019-13777-z

[66] Gambarotta, S., Arena, F., Floriani, C., Zanazzi, P.F.: Carbon dioxide fixation: Bifunctional complexes containing acidic and basic sites working as reversible carriers. J. Am. Chem. Soc. **104**(19), 5082–5092 (1982). https://doi.org/10.1021/ja00383a015

[67] Benn, E.E., Gaskey, B., Erlebacher, J.D.: Suppression of hydrogen evolution by oxygen reduction in nanoporous electrocatalysts. J. Am. Chem. Soc. **139**(10), 3663–3668 (2017). https://doi.org/10.1021/jacs.6b10855

[68] Chen, W., Liao, L.W., Cai, J., Chen, Y.-X., Stimming, U.: Unraveling complex electrode processes by differential electrochemical mass spectrometry and the rotating ring-disk electrode technique. J. Phys. Chem. C **123**(49), 29630–29637 (2019). https://doi.org/10.1021/acs.jpcc.9b09952

[69] Bondue, C.J., Graf, M., Goyal, A., Koper, M.T.M.: Suppression of hydrogen evolution in acidic electrolytes by electrochemical co_2 reduction. J. Am. Chem. Soc. **143**(1), 279–285 (2021). https://doi.org/10.1021/jacs.0c10397

[70] Wuttig, A., Surendranath, Y.: Impurity ion complexation enhances carbon dioxide reduction catalysis. ACS Catal. **5**, 4479–4484 (2015). https://doi.org/10.1021/acscatal.5b00808

[71] Shang, H., Wallentine, S.K., Hofmann, D.M., Zhu, Q., Murphy, C.J., Baker, L.R.: Effect of surface ligands on gold nanocatalysts for co_2 reduction. Chem. Sci. **11**, 12298–12306 (2020). https://doi.org/10.1039/D0SC05089J

[72] Mezzavilla, S., Horch, S., Stephens, I.E.L., Seger, B., Chorkendorff, I.: Structure sensitivity in the electrocatalytic reduction of CO_2 with gold catalysts. Angew. Chem. Inter. Ed. **58**(12), 3774–3778 (2019). https://doi.org/10.1002/anie.201811422

[73] Gunathunge, C.M., Li, J., Li, X., Waegele, M.M.: Surface-adsorbed CO

as an infrared probe of electrocatalytic interfaces. ACS Catal. **10**(20), 11700–11711 (2020). https://doi.org/10.1021/acscatal.0c03316

[74] Gunathunge, C.M., Li, J., Li, X., Hong, J.J., Waegele, M.M.: Revealing the predominant surface facets of rough Cu electrodes under electrochemical conditions. ACS Catal. **10**(0), 6908–6923 (2020) https://doi.org/10.1021/acscatal.9b05532. https://doi.org/10.1021/acscatal.9b05532

[75] Dunwell, M., Yang, X., Yan, Y., Xu, B.: Potential routes and mitigation strategies for contamination in interfacial specific infrared spectroelectrochemical studies. J. Phys. Chem. C **122**(43), 24658–24664 (2018). https://doi.org/10.1021/acs.jpcc.8b05634

[76] Cave, E.R., Montoya, J.H., Kuhl, K.P., Abram, D.N., Hatsukade, T., Shi, C., Hahn, C., Nørskov, J.K., Jaramillo, T.F.: Electrochemical CO_2 reduction on au surfaces: Mechanistic aspects regarding the formation of major and minor products. Phys. Chem. Chem. Phys. **19**, 15856–15863 (2017). https://doi.org/10.1039/C7CP02855E

[77] Marcus, Y.: Ion Properties. Marcel Dekker, Inc., New York, NY (1997)